

Lawrence Berkeley National Laboratory

LBL Publications

Title

Mechanical analysis of the Nb 3 Sn 11 T dipole short models for the High Luminosity Large Hadron Collider

Permalink

<https://escholarship.org/uc/item/6ww3t420>

Journal

Superconductor Science and Technology, 32(8)

ISSN

0953-2048

Authors

Izquierdo Bermudez, S
Nilsson, E
Bottura, L
[et al.](#)

Publication Date

2019-08-01

DOI

10.1088/1361-6668/ab1f39

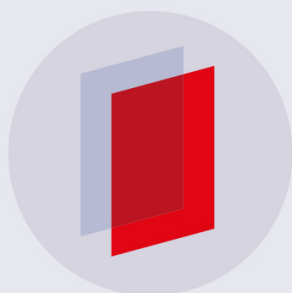
Peer reviewed

PAPER

Mechanical analysis of the Nb₃Sn 11 T dipole short models for the High Luminosity Large Hadron Collider

To cite this article: S Izquierdo Bermudez *et al* 2019 *Supercond. Sci. Technol.* **32** 085012

View the [article online](#) for updates and enhancements.



IOP | ebooks™

Bringing you innovative digital publishing with leading voices to create your essential collection of books in STEM research.

Start exploring the collection - download the first chapter of every title for free.

Mechanical analysis of the Nb₃Sn 11 T dipole short models for the High Luminosity Large Hadron Collider

S Izquierdo Bermudez , E Nilsson, L Bottura, N Bourcey, A Devred, P Ferracin, S Ferradas Troitino, L Fiscarelli, M Guinchard, C Löffler , J Mazet, J C Perez, H Prin, F Savary, S Sequeira Tavares, G Vallone and G Willering

CERN, 1211 Geneva, Switzerland

E-mail: susana.izquierdo.bermudez@cern.ch

Received 22 February 2019, revised 10 April 2019

Accepted for publication 3 May 2019

Published 16 July 2019



CrossMark

Abstract

For the Large Hadron Collider luminosity upgrade, two of the NbTi 8.3 T main bending dipoles will be replaced by two shorter Nb₃Sn 11.2 T dipoles to create space for the installation of collimators in the dispersion suppression region. With the aim to verify the design features, several 2 m long 11 T models have been constructed and tested at CERN. During the fabrication and assembly of, so far, seven single and two double aperture short model magnets, several challenges were identified and tackled. These include reproducibility in coil fabrication and assembly procedure, as well as control of mechanical stresses in the conductor and surrounding structure. In order to limit coil over-compression and improve reproducibility, the cable insulation was re-optimized. In addition, a review of the collaring procedure of the 11 T magnet was launched with the goal of reducing the risk of conductor degradation due to excessive stress. In this paper, the main fabrication and assembly steps are described, including the description of the actions taken to resolve the identified weakness.

Keywords: high luminosity LHC, high field Nb₃Sn magnet, 11T dipole

(Some figures may appear in colour only in the online journal)

1. Introduction

In order to create space for the installation of collimators in the dispersion suppressors, two standard LHC NbTi dipoles (MB) will be replaced with shorter Nb₃Sn magnets with field of 11 T (MBH) [1]. A higher field allows for shorter magnets and room for collimator units, necessary for the High Luminosity upgrade of the Large Hadron Collider (HL-LHC). The installation of the 11 T dipole marks the start of a new era in particle accelerators, as it is the first time accelerator magnets relying on Nb₃Sn are installed in the LHC. With aperture of 60 mm, magnetic length of 5.3 m and bore field of 11.2 T, these two layer cosine-theta dipoles will operate at 80% of the load line. The nominal (I_{nom}) and ultimate (I_{ult}) current of the 11 T dipole is 11.85 kA and 12.85 kA respectively. After an initial pre-study [2], CERN and FNAL started

a joint development program to design and build 2 m long single and double aperture demonstrators [3, 4]. At CERN, seven short single aperture (SP101-SP107) and two double aperture model magnets (DP101-DP102) were built so far to verify the technology choices. Table 1 summarizes the coils assembled in each magnet, including the conductor type and test date (note that some of the coils were used for several magnet assemblies).

One of the main challenges is the brittleness of the Nb₃Sn conductor [5–7]. The assembly process is delicate as there is a risk of over compressing the coil in its collared coil structure. In addition, fabrication of Nb₃Sn coils requires heat treatment and impregnation, which needs to be well controlled. At powering, the Lorentz forces in the coil are directed towards the mid-plane (see figure 2) and radially outwards. Displacement of the turns at powering could compromise field

Table 1. Overview on tested magnets.

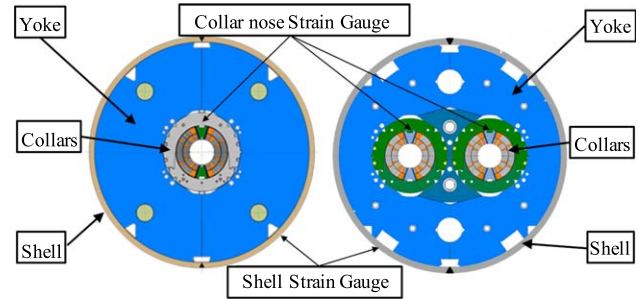
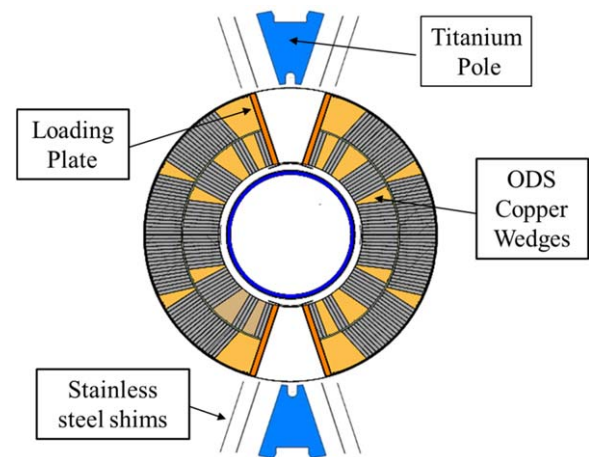
Magnet	Collared coil	Coil	Conductor	Test date
SP101	CC101	106	RRP 108/127	October–December 2014
SP102	CC102	106	RRP 108/127	May–June 2015
SP103	CC103	108	RRP 132/169	September–October 2015
		111	RRP 132/169	
DP101	CC102	106	RRP 108/127	December 2015–March 2016
		108	RRP 132/169	
SP104	CC104	109	RRP 132/169	June–July 2016
		111	RRP 132/169	
SP105	CC105	112	RRP 132/169	November 2016
		113	RRP 132/169	
DP102	CC104b	109	RRP 132/169	October–November 2017
		112	RRP 132/169	
		115	RRP 150/169	
SP106	CC105b	114	RRP 150/169	December 2017–March 2018
		115	RRP 150/169	
SP107	CC106	116	RRP 150/169	July 2018
		117	RRP 150/169	
SP107	CC107	120	RRP 108/127	
		121	RRP 108/127	

RRP: restacked-rod process.

quality and cause releases of frictional energy, which could trigger a quench. Pre-load is applied to the coil in the azimuthal direction in order to avoid displacement of the conductors. The design criteria used for Tevatron dipoles [8], HERA dipoles [9], RHIC dipoles [10], SSC dipoles [11, 12], LHC dipoles [13], HL-LHC Nb₃Sn magnets [14], and presently used for Nb₃Sn magnets for the FCC study [15] aim in the design phase at a pre-load still keeping contact between pole and coil at nominal current. This requirement was set at the beginning of the accelerator magnet era [16].

The mechanical design of the 11 T relies on separate stainless steel collars for each aperture and a vertically split iron yoke, surrounded by a welded stainless steel shell (see figure 1). Two different concepts for coil pre-load were explored. In FNAL design, poles are impregnated with the coil and the pre-load is provided through coil-mid-plane shimming and horizontal deformation of the collared coils during the cold mass assembly [4]. CERN pursued a solution with removable poles [3], allowing the loading at the poles similarly to the conventional collared NbTi accelerator magnets [9–13] and some earlier Nb₃Sn magnets [17, 18]. The pre-load results mainly from the interference of a removable pole, made up of titanium, with the *coil package*, which consists of the coil and of lateral stainless steel shims of adjustable thickness (see figure 2).

In the 11 T dipole the stress sensitive Nb₃Sn conductor operates with both high stresses on the mid-plane and nearly no compression at the pole when powered [19]. The models SP104, SP105 and DP102 have all been limited at the mid-plane below ultimate current [20]. Through the short model

**Figure 1.** 11 T single (left) and double (right) aperture magnet cross section including the location of the strain gauges.**Figure 2.** Coil package, including removable pole and loading shims.

program, it has become clear, from both mechanical measurements and predicted stresses by finite element (FE) modelling, that there is a risk of over compressing the coils during the collaring procedure. Measurements on conductor samples, which have been submitted to room temperature transverse stress cycles representative of what they experience during the collaring process have shown that performance degradation starts to occur when exceeding 150 MPa [21]. The risk has been minimized by a revisited collaring procedure and a reduced target excess, ensuring that the coils are assembled without over compressing the conductor. Two short models have been built using this new collaring procedure. These models, SP106 and SP107, both reached ultimate current without any observed limitation at the mid-plane. In this paper, a description of the coil fabrication and magnet assembly process of the short models developed at CERN is provided and the mechanical measurements during assembly, cool down and powering are summarized.

2. Magnet design

The 11 T coils are made with a Rutherford-type cable composed of 40 strands of 0.70 mm diameter. The cable incorporates a 12 mm wide stainless steel core of 25 μ m thickness to reduce inter-strand coupling currents. Each coil has

Table 2. Cable, coil and magnet parameters.

Parameter	Unit	
Strand diameter	mm	0.70
Number of strands in cable		40
Cable bare width (before/after HT)	mm	14.70/14.85
Cable bare mid-thickness (before/after HT)	mm	1.250/1.307
Keystone angle (before/after HT)	degrees	0.79/0.81
Insulation thickness per side at 5 MPa	μm	100
Coil clear aperture diameter	mm	60
Magnet (LHe vessel) outer diameter	mm	532/570
Number of turns in layer 1/2 (quadrant)		22/34
Operational temperature T_{op}	K	1.9
Nominal field B_{nom} for single/double aperture	T	11.20/11.23
Nominal current I_{nom}	kA	11.85
Peak field B_p at I_{nom} for single/double aperture	T	11.97/11.77
I_{nom}/I_{ss} at 1.9 K for single/double aperture	%	81/80
Ultimate field B_{ult} for single/double aperture	T	12.03/12.15
Ultimate current I_{ult}	kA	12.85
I_{ult}/I_{ss} at 1.9 K for single/double aperture	%	88/87
Stored energy at I_{nom} for single/double aperture	MJ m^{-1}	0.44/0.90
Inductance at I_{nom} for single/double apert.	mH m^{-1}	5.7/11.9
F_x/F_y (per quadrant) at I_{nom}	MN m^{-1}	3.64/-1.86
F_θ layer 1/layer 2 (per quadrant)	MN m^{-1}	1.26/1.69
F_z (per aperture) at I_{nom}	MN	0.44

56 turns, 22 in the inner layer and 34 in the outer layer. The magnetic length of the short model magnets is 1.7 m. Table 2 summarizes the main cable, coil and magnet parameters for the single and double aperture magnets.

The main fabrication and assembly steps are as follows: the coil is wound and cured while the cable is still ductile, then the coil is reacted into Nb_3Sn through heat treatment in a furnace. Finally, the coils are impregnated with epoxy CTD-101K resin. The arc length and radial dimension of the coils are measured every 100 mm using a coordinate measurement machine (CMM) [22]. The deviation of the azimuthal dimensions with respect to the nominal values is estimated by aligning the data on the nominal outer radius (60.8 mm). As a function of the azimuthal size of the coils in the assembly, the pre-stress is fine-tuned by applying stainless steel shims at the interface of the pole and the loading plate of the coil. The stresses were initially predicted with 2D FE modelling and the shimming plan is based on the solution that satisfies our stress allowance in the conductor blocks at all assembly steps and powering. Results presented in this paper are based on a 2D ANSYS APDL model. Exploiting the problem symmetry, only a quarter of the magnet is simulated, assuming plane stress conditions. All materials are assumed to remain in the elastic regime. The coil is modelled as a block with uniform properties. All coil components are glued, and contact

elements with sliding and separation allowed are used for the coil to pole interface. For the rest of the interfaces (between the coils, between the coils and structural components and between structural components), frictional contacts are considered, assuming a friction coefficient of 0.2.

For the latest assemblies (SP107 and onward), extensive collaring trials were carried out on a mock-up to qualify the FE modelling and derive pragmatic criterions [23]. The finest thickness of the shims is $25 \mu\text{m}$, which allows control of the pre-stress levels to 10 MPa on average. The coil pair is enclosed in 3 cm thick stainless steel collars. The role of the collars is to confine and compress the coils radially and azimuthally. The coils are collared in a hydraulic press with a maximum capacity of 20 MN m^{-1} . At maximum pressure, the keys are inserted, locking the collars around the coil assembly. Subsequently, the press is released and the collared coil assembly experiences a relaxation. The most deleterious conditions for the mid-plane Nb_3Sn conductor occur at the time of the collaring. The collared coils are then assembled to single or double aperture magnets with a vertically split yoke and a stainless steel shell (see figure 1).

As a final step in the assembly, end plates are mounted and welded. The short models are equipped with strain gauges on the collar nose that measure the strain in vertical (or radial) direction. There are three instrumented collar packs per aperture in the straight section of the magnets: near each extremity (connection and non-connection side) and in the central region. The stresses in the coil are about half of the stresses measured on the collar nose, as has recently been experimentally validated by collaring tests on shorter coil segments [23]. Five of the magnets (SP101, SP103, SP107, DP101 and DP102) have strain gauges on the inner and outer radius of the shell. The magnet extremities are equipped with four bullet gauges per aperture. One of the main objectives of the 11 T short model program is to determine the optimal pre-stress for the coils.

3. Overview of magnet performance

Table 3 summarizes the training performance of the seven single and two double aperture magnets tested. The detailed training performance of each individual magnet is shown in appendix. The cold powering tests of all magnets except SP106 starts with a training campaign at 1.9 K, which is the foreseen operating temperature of this magnet in the LHC. In SP016 the initial training was done at 4.5 K due to temporary limitations of the test station. The first quench of all single aperture magnets was between 7.5 and 10.4 kA, which corresponds to 55 to 72% of the short sample limit. The first model, SP101, reached nominal current in 18 quenches but then showed detraining quenches and limited performance in the transition between the inner and outer layer (the so-called layer jump) of coil 107. The collared coil was disassembled and coil 107 was replaced by a virgin coil (coil 108) in the so-called SP102. SP102 and SP103 were tested up to a target of 12.8 kA since the collared coils were to be reused in double aperture configuration, reaching nominal current in 7 and 14

Table 3. Magnet performance.

Magnet	I_{ss}		First training quench		Maximum current during training with standard ramp rate		# Quenches to reach I_{nom}	Limitation
	1.9 K [kA]	4.3 K [kA]	T [K]	I_{1st} [kA]	$I_{max, 1.9 K}$ [kA]	$I_{max, 4.5 K}$ [kA]		
SP101	14.39	12.86	1.9	9.31	11.92	11.20	18	Layer jump coil 107
SP102	14.50	13.05	1.9	8.07	12.79 ^a	11.70	7	—
SP103	14.15	12.78	1.9	9.00	12.85 ^a	11.74	14	—
SP104	14.40	13.04	1.9	8.00	11.73	11.41	—	Layer jump coil 113 ^b
SP105	14.63	13.25	1.9	7.90	12.37	11.30	—	Mid-plane
SP106	14.83	13.55	4.5	9.26	13.46	11.66	25 ^c	—
SP107	14.42	13.10	1.9	10.43	12.85 ^a	12.28	5	—
DP101	14.06	12.73	1.9	12.15	13.21	—	0	—
DP102	14.45	13.04	1.9	11.38	11.39	10.42	—	Mid-plane

^a Test target: no attempts to train higher.

^b Layer jump limitation overpass with V-shaped cycles, quenching in the coil mid-plane at 12.25 kA.

^c Initial training at 4.5 K.

quenches respectively. Since one of the coils in SP102 (coil 106) was already tested in SP101, the training of the aperture is biased. At 4.5 K, the maximum current reached in SP102 and SP103 corresponds to 81%–83% of the short sample limit [24]. SP102 demonstrated that a coil can reach ultimate current after a de-collaring and re-collaring cycle. The single aperture magnets SP102 and SP103 were disassembled and the collared coils were assembled in the first double aperture magnet DP101. The magnet reached 12.2 kA in the first training quench, showing very good memory also after disassembly and reassembly of the collared coils. The magnet reached 94% of its short sample limit at 1.9 K. SP102, SP103 and DP101 showed stable operation at ultimate current [25]. The next magnet tested, SP104, was limited in the layer jump of coil 113. The limitation was overpassed by ramping using the so-called V-shaped cycles, designed to invert induced coupling currents. Current was ramped at 50 A s^{-1} to a level just below quench, left at this current for 10 min, followed by a ramp down and immediate ramp up at high ramp rate ($100\text{--}200 \text{ A s}^{-1}$). The maximum reached current was 12.25 kA. At maximum current, the magnet was consistently quenching in the mid-plane [20]. SP105 was also limited on the mid-plane, at 12.4 kA (85% of its short sample limit). This was interpreted as a sign of excessive stress, so the magnets were disassembled and re-collared with lower pre-stress in CC104b and CC105b. In addition, coil 113 was replaced by coil 109 in CC104b. In spite of the reduced azimuthal excess, the coils of DP102 were limited on the mid-plane, which indicated that the coils have been permanently damaged prior to this cold test. The magnet was limited at 80% of its short sample limit both at 1.9 K and 4.5 K. The magnet reached its plateau current in the first quench, confirming the good memory after complete disassembly. Target pre-stress was reduced for subsequent disassemblies. During the initial training campaign at 4.5 K, SP106 reached a maximum current of 11.46 kA (86% of I_{ss}). Only after thermal cycle at 1.9 K nominal current was reached. SP106 reached 13.5 kA at

1.9 K (91% of I_{ss}) after a series of so-called high MIITs tests [26], with no limitations on the mid-plane and stable operation at ultimate current. During high MIITs tests, the quench protection system is delayed and a high quench load is deposited in the magnet to explore the magnet limits in terms of hot spot temperature. SP107 reached nominal current after 5 quenches, the fastest training so far, and showed stable operation at ultimate current with no limitations on the mid-plane. SP107 was not trained above ultimate current at 1.9 K, but reached 94% of its short sample limit at 4.5 K.

4. Cable insulation

The cable insulation consists of a C-shaped glass/mica foil folded around the cable, and braided with S-2 11-Tex glass fibre (see figure 3). A similar insulation scheme was used in [18]. The target insulation thickness is $100 \mu\text{m}$. The measured insulation thickness at 5 MPa for coils 105 to 117 is $130\text{--}135 \mu\text{m}$, which translates to an over-thickness per coil quadrant in the azimuthal direction of 2 mm in the outer layer and 1.3 mm in the inner layer. This over-thickness resulted in difficulties in closing the heat treatment and vacuum impregnation molds and in the observations of large coil spring back at the opening of the heat treatment mold. It was also found that the C-shaped glass/mica wrapped around the cable, with a gap of approximately 7 mm in the middle, is a potential stress intensifier at the cable edge. This was first observed in a collaring test for aperture SP105b, where pressure measurement films were installed in the coil mid-plane. Figure 4 shows the imprints of the Fuji film. The stress peaks at the edges of the cable are clear, in correspondence with the edges of the mica wrap. The stress in the center of the cable, where the mica foil has a gap, is at least two times lower than the stress at the edges. In order to better quantify the role of the C-shaped glass/mica foil, the high compaction in the 11 T coils due to insulation over-thickness and the

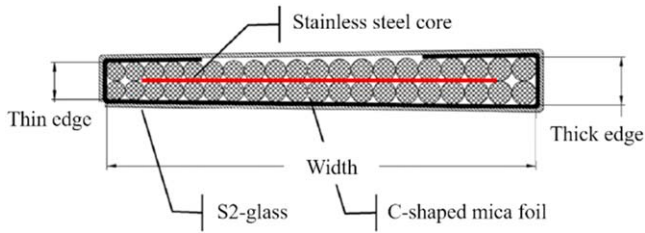


Figure 3. Cross section of an 11 T insulated cable: in dark black, the mica foil.

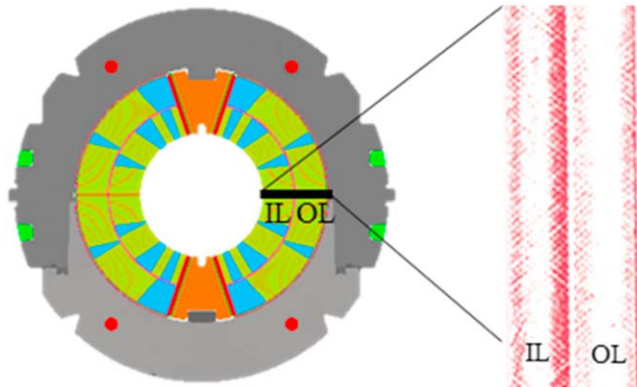


Figure 4. Pressure measurement film (Fuji-paper) imprints obtained during collaring tests in single aperture model SP105b in the inner (IL) and outer layer (OL) mid planes. Pressure range 50–130 MPa.

effect of the cable keystone angle, pressure tests were done in SMC-11 T racetrack coils wound with non-keystone cable. Among the different coils built [27], a coil insulated with only braided S-2 glass and a coil insulated with the 11 T insulation scheme (C-shaped glass/mica 25 mm width (7 mm gap) and braided glass) were selected for these tests. Figure 5 compares pressure sensitive imprints for a coil wound with and without C-shaped mica foil under an average compression of 50 MPa at room temperature. The effect of the mica foil is also present in coils wound with non-keystone cable under a uniaxial state of compression. In the case of SMC-11 T, the pressure is distributed over ~85% of the cable surface in the presence of mica. For the 11 T coils in a typical collaring cycle, the pressure is above 10 MPa only in 60%–70% of the cable surface, and 5% of the cable is above 130 MPa. The conclusion is that around half of the stress heterogeneity in the mid-plane of the 11 T coils is caused by the C-shaped glass/mica. The rest can be related to the different rigidity of the inner and outer edge of the keystone cable, the high compaction of the coils due to the insulated conductor over-thickness and the non-uniaxial loading of the coils in the collared coil structure.

In order to cope with the high compaction and the stress concentration on the cable edges, the cable insulation scheme was re-optimized from coil 118. Braiding parameters were modified in order to reach the target insulation thickness of 100 μm at 5 MPa. Table 4 summarizes the braiding parameters for the different 11 T coils and figure 6 shows the braid on

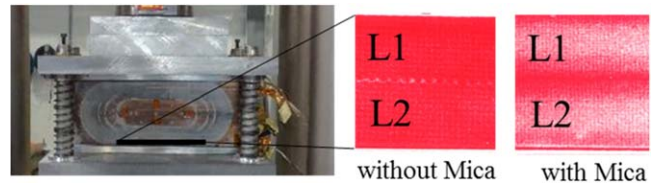


Figure 5. Pressure measurement film (Fuji-paper) imprints obtained during a room temperature test in SMC-11 T coils wound with cable insulated with and without C-shaped mica foil, for an average pressure of 50 MPa. Pressure range of the Fuji film 10–50 MPa.

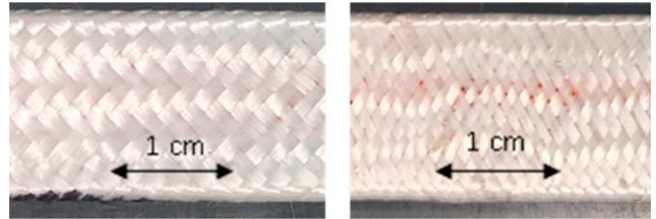


Figure 6. Braid on insulation for coils 108–117 (left) and for all coils built after coil 118 (right).

Table 4. Key braided-on insulation parameters.

Parameters	Coils 105–107	Coils 108–117	From coil 118
Strand	11 TEX (636)	11 TEX (636)	11 TEX (636)
# Carriers	32	32	32
# Plies/strand	9	9	4
Picks per cm	7	6	9
Insulation thickness at 5 MPa, μm	130–135	130–135	100–110
Glass/mica foil width, mm	25	25	31

insulation for the original and optimized insulation layout. In order to minimize the C-shaped mica contribution, the width of the mica tape was increased from 25 to 31 mm, reducing the gap in the middle of the cable from 7 to 1 mm. Mechanical measurements on coil segments show a negligible impact of the insulation layout on the coil stiffness [28].

5. Coil fabrication

The coil fabrication is based on the wind-and-react technology where the superconducting phase is formed after winding and during coil high-temperature heat treatment. The cable is wound around a titanium pole keeping a tension on the cable of 20 kg. Gaps are placed between pole segments to allow the coil to contract in the longitudinal direction from the winding tension and from the conductor contraction during heat treatment. Pole gaps closed 0.6–1.3 mm m⁻¹ during reaction for coils 118–123. Previous coils show a negligible difference

Table 5. Nominal (Nom.) and measured (Meas.) radial dimensions of the reaction and impregnation mold.

Parameters	Reaction mold		Impregnation mold	
	Nom.	Meas.	Nom.	Meas.
Mold inner radius (IR), mm	29.75	29.74	29.775	29.81
Filler thickness in IR, mm	0.25 ^a	0.25	0.1 ^c	0.03
Coil IR, mm	—	—	29.9	—
Insulated conductor IR, mm	30	—	30	—
Insulated conductor outer radius (OR), mm	60.6	—	60.6	—
Coil OR, mm	—	—	60.8	—
Filler thickness in OR, mm	0.3 + 0.125 ^b	—	0.5 + 0.1 ^d	0.475 + 0.03
Mold OR, mm	61.25	61.245	61.425	61.435

^a One layer of mica.^b Stainless steel sheet and one layer of mica.^c Demolding film or Teflon coating.^d Stainless steel sheet and demolding film or Teflon coating.

on pole gaps before and after heat treatment, except in coils 115 and 116 where the pole gap increases by 1.5 mm m^{-1} and 0.8 mm m^{-1} respectively. This is interpreted as a sign of large coil compaction in the azimuthal direction due to the over-thickness of the conductor insulation. The material for the wedges in between conductor blocks is an oxide dispersion strengthened copper alloy (Discup C3/30 OD [29]), which instead of suffering a full annealing at the reaction temperature ($\sim 650^\circ\text{C}$), maintains most of its strength because the oxide dispersion prevents the grain growth. Wedges were split in two segments for the first coils, but from coil 111 full length wedges are used for the short model coils. The inner and outer layers are wound without a splice between them, using a single piece of insulated Rutherford cable. When the inner layer is wound, polymer-derived ceramic binder (CTD-1202) is applied to the S2 glass insulation of the cables and cured in two steps, first at 80°C for 1 h, then at 170°C for 3 h. The aim of the curing is to provide a rigid coil for handling and to ensure a suitable reference surface for the winding of the outer layer. After winding the outer layer, binder is applied to the outer layer and the whole coil is cured. The curing cavity size is equal to the final coil cavity size.

After winding and curing, coils are reacted in oxygen free, gas tight oven using an argon gas atmosphere. The heat treatment cycle uses three temperature plateaus of 210°C , 400°C and 650°C with a duration of 48 h, 48 h and 50 h respectively. The heat treatment has been optimized to meet both minimum I_c and RRR targets [30]. The temperature homogeneity during the plateaus is typically better than 5°C . Before transferring the reacted coil in the impregnation mold, a 0.1 mm thick S2 glass sheet and printed circuits (traces) with quench heaters and voltage taps are placed on top of the outer layer and connected. This process was implemented from coil 114. In earlier coils (coils 106–113), traces were glued on the outer surface of the coil after impregnation. In the inner diameter of the coil, a 0.1 mm thick S2 glass sheet is installed. Table 5 summarizes the radial dimensions of the reaction and impregnation mold, comparing when available the nominal to the measured dimensions. Superconducting NbTi cable leads are soldered to the reacted Nb_3Sn coil leads

**Figure 7.** View of an 11 T coil after impregnation.

with 4/96 Sn–Ag solder and a non-activated flux, MOB 39. The stainless steel end saddles are replaced by G11 parts to improve the electrical insulation at the level of the splice and quench heater leads (see figure 7). Vacuum impregnation is done with CTD-101K epoxy. External heat cartridges are used on the outer surface of the tooling to reach and maintain the target temperatures for each step. The coil, inside the impregnation mold, is placed in the impregnation chamber and heated to 60°C under vacuum to evacuate any volatiles. It requires about 4–5 d for the pressure in the impregnation mold to reach about 0.3 mbar (chamber at 0.003 mbar), after which the coil is considered ready for impregnation. The epoxy is mixed and degassed under agitation at 60°C and at lower pressure level than the coil. The mixing tank pressure is increased to 400 mbar to inject the resin in the mold, at a temperature of approximately 60°C . The coil is fully impregnated in about 3 h, and the vacuum chamber is set to atmospheric pressure. To insure any small voids are collapsed, the impregnation mold is then held under 2 bars pressure at 80°C for 8 h, hence initiating the curing of the resin. The standard curing cycle is then applied, and is composed by two plateaus, the first at 110°C for 6 h and the second at 125°C for 16 h.

At the end of the coil manufacturing process, the arc length and radial dimension of the coils are measured at every 100 mm using a CMM. By aligning the data on the nominal

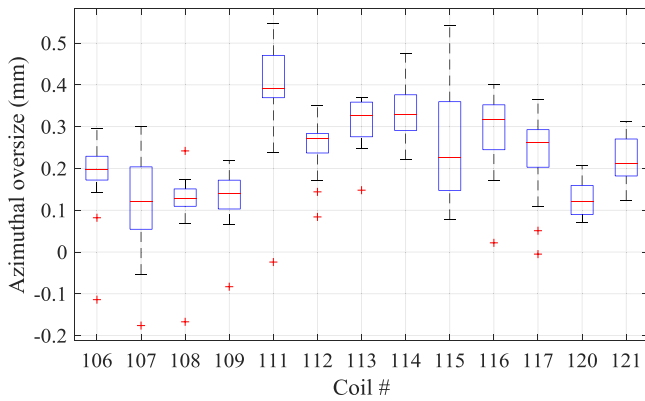


Figure 8. Coil azimuthal size deviation with respect to nominal. Each box represents the eight cross sections measured per coil: the central line corresponds to the median, the edges of the box are the 25th and the 75th percentiles and the whiskers extend to the extreme data points. Outliers are represented with a red cross.

outer radius of the impregnated coil (60.8 mm), it is possible to estimate the deviations of the azimuthal dimensions with respect to the nominal values. A great challenge in the short model program is to produce uniform coils. Figure 8 summarizes the azimuthal coil size deviation (left + right mid-plane) in the tested coils. The horizontal lines indicate the minimum, the 25% percentile, the median, the 75% percentile, and the maximum deviations. The short coils have a size variation along the length up to 0.550 mm, and a median value ranging from 0.100 to 0.400 mm. The large size variation along the length has proven to lead to varying stresses on the conductor along the magnet length. MQXF short model coils show a significant lower size variation along the magnet length (0.250 mm), and a median value ranging from -0.200 to $+0.250$ mm. This is comparable to the values achieved in the coils with the new insulation layout (coils 120 and 121), pointing to the idea that the large compaction of the 11 T coils in the impregnation mold had a detrimental effect on the coil azimuthal size. Prototype coils produced by the US Accelerator Research Program (AUP) are within -0.100 mm to $+0.000$ mm the average size, with a longitudinal variation of ± 0.050 mm [31]. In the LHC dipoles the azimuthal coil size has been controlled within 0.15 mm, nevertheless, the spread in the coil position evaluated from the magnetic measurements is at least a factor of three lower [32]. Measurements of the coil size before and after powering show that the coils do not adjust in terms of size through the full assembly and test. The difference on coil azimuthal size after coil fabrication and after cold powering test is lower than $40 \mu\text{m}$.

6. Coil pack assembly

Coils are paired together and the pre-stress is fixed by applying stainless steel shims at the interface of the pole and the coil loading plate. The coil excess is defined as the interference that each quadrant of the coil (including azimuthal shims, loading plate and ground insulation) has with

Table 6. Coil package excess per quadrant [mm].

Collared coil	Average	Minimum	Maximum
CC102	0.299	0.155	0.338
CC103	0.381	0.223	0.434
CC104	0.441	0.358	0.480
CC105	0.350	0.288	0.450
CC105b	0.300	0.238	0.400
CC104b	0.344	0.250	0.381
CC106	0.329	0.218	0.391
CC107	0.211	0.181	0.247

respect to the nominal cavity of the collars. The excess is therefore a parameter proportional to pre-compression of the coils inside of the collars. The average, maximum and minimum coil package excess per quadrant with respect to the nominal cavity of the collars, including lateral stainless steel shims, for the tested short models in chronological order, are summarized in table 6. As showed in table 6, the azimuthal excess of the paired coils deviate by up to 0.17 mm per quadrant along the magnet length. As stresses on the conductor in assembly and powering depend on the local coil package size, it is challenging to provide adequate pre-stress along the magnet length for coils that vary in size. There is a risk of local under- or over-compression of the conductor. SP104 is the magnet with the highest azimuthal excess, i.e. the highest pre-stress. As its performance was limited in the coil mid-plane at 12.30 kA [20], the pre-load in the following magnets was decreased. SP105 was limited on the mid-plane at 12.40 kA. Even though its average azimuthal excess per quadrant was 0.35 mm, its large variation in coil size along the magnet length lead to azimuthal excess in the central region similar to that of SP104 (see table 6). Coils from these limited assemblies were reused in a double aperture configuration (DP102), this time assembled with lower pre-stress in both apertures (CC104b and CC105b), with the aim to reduce the stresses on the mid-plane. In spite of the reduced azimuthal excess, the coils of DP102 were limited on the mid-plane. SP106 was assembled with an average excess of 0.330 mm, re-using collars from the disassembled SP105. Measurements on these collars after test show that the collars were plastically deformed. The collar cavity size was up to $60 \mu\text{m}$ larger than nominal in the azimuthal direction, meaning that the effective excess in SP106 was 0.270 mm instead of 0.330 mm. SP107 the maximum excess was chosen to be 0.250 mm, resulting in an average excess of 0.210 mm.

7. Collared coil assembly

7.1. Collaring procedure

The role of the laminated collars is to fix and close the coils in a precise cavity. When the collars are placed around the coil pair without any compression, the key slots are misaligned by 0.15 mm, see figure 9. The key slots are aligned by pressurizing the collar-coil assembly in a hydraulic press with a

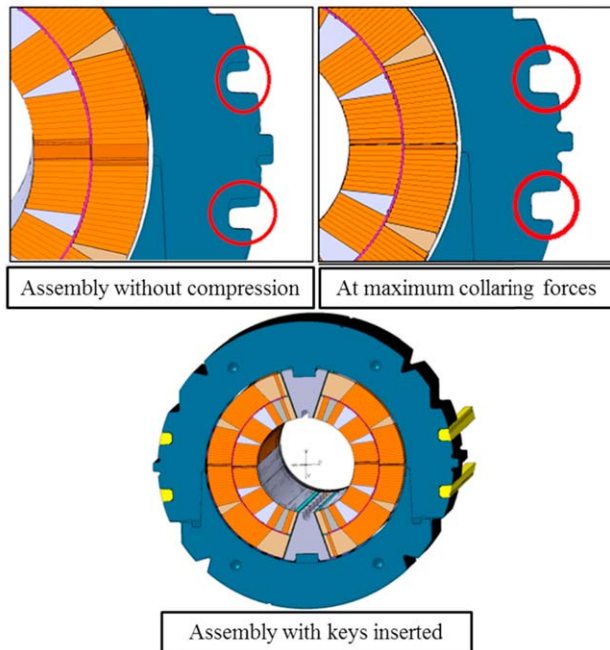


Figure 9. Illustration of the collared coil assembly without compression, with an interference of the key slots of 0.15 mm and the assembly under compression at which the key slots are aligned.

capacity of 20 MN m^{-1} over the 2 m length. At a relative displacement of about 0.15 mm of the upper and lower collars, the required clearance is achieved, the keys are inserted and the press is released. The collar-coil assembly will experience a release of stresses at removal of the collaring press force. This process of fully opening the keyways in order to drive the keys in leads to an overshoot of stresses in the collar-coil assembly, with respect to the targeted pre-stress at room temperature. It is at this time that the coil mid-plane turns experience the highest stress.

Along the short model program, there were several indications that excessive force was applied in the collaring procedure. The main indications were the plastified edges on collars observed in profile measurements in SP105 after cold tests and the irreversible degradation of performance at mid-plane on several magnets [20]. The assembly step where the coil sees the highest stresses is during collaring, when the collared coil is compressed in the collaring press. To avoid excessive stresses in the coil at room temperature it was decided to revisit the collaring procedure.

In order to avoid excessive stress, and to ensure a smooth transition of the force from the hydraulic collaring press to the coil assembly, stoppers are placed between the assembly and the press beams on the right and left side, see figure 10. The stoppers stabilize the force distribution between the left and right coil branch. The height of the stoppers can be modified with a shim, referred to as the collaring tool shim. In the early assemblies (the collared coils of SP101, SP102 and SP103), the collaring tool shim was 0.40 mm, with a total stopper height of 70.1 mm for a collaring cavity 70 mm height (see table 7), resulting on a clearance for key insertion of

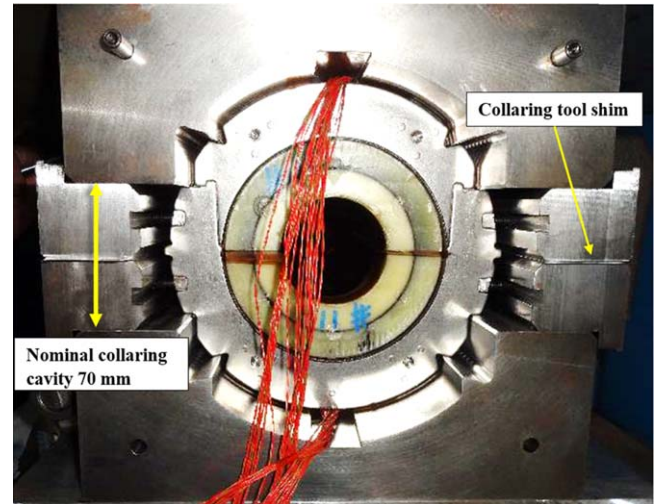


Figure 10. Illustration of the collared coil assembly without compression, with an interference of the key slots of 0.15 mm and the assembly under compression at which the key slots are aligned.

–0.100 mm. The required clearance for key insertion (around 0.150 mm) was achieved through the deformation of the collaring tool and stoppers. This was achieved applying a large collaring force (34 MN). For SP104 key insertion was not feasible for these collaring tool parameters. Therefore, the collaring tool shim was reduced to 0.15 mm and the keys were inserted at 20 MN. Also in the collaring of SP105 and the two-collared coils of DP102 a stopper shim of 0.15 mm was used. At the time, it was not yet understood how sensitive the coils are to the forces applied in the collaring procedure. Since then it has been confirmed through extensive tests on short coil segments that unnecessary high pressure was applied to the assemblies [23]. One indication is that SP104b and SP105b were de-collared under less than half of the force used to collar them (see table 7). The stresses in the coils during the collaring procedure have recently been quantified in mock-up tests using 150 mm coil segments. A linear relation is found between collar nose and pole turn stress in the mock-up tests. Collaring of the coil segments also show that collars are plasticized for azimuthal excess beyond $350 \mu\text{m}$ per quadrant, which may lead to a loss in linearity between the collar nose and pole stress [23].

With the sensitivity of the coils in mind, instead of targeting a predefined collaring press force and cavity, it was decided to base the required collaring force on the displacement of the collars needed to align the collaring slots such that the keys can be inserted. The alignment of the key slots are controlled by monitoring the length of the stoppers while applying the collaring forces, using LVDT sensors on three locations along the length on each side. With this new method collaring was achieved at only 10 MN in SP106, the lowest collaring force so far, with the lowest strain measured in the short models at peak collaring force (see peak stress in figure 11). SP107 was collared using the same principle. SP106 and SP107 were also the assemblies collared with the lower excess.

Table 7. Collaring parameters for the short model magnets.

	Parameter	CC101	CC102	CC103	CC104	CC105	CC104b	CC105b	CC106	CC107
Collaring	Nominal collaring cavity, mm	70.0	70.0	70.0	70.0	70.0	70.0	70.0	70.0	70.0
	Stopper height, including shims, mm	70.1	70.1	70.1	69.85	69.85	69.85	69.85	69.85	69.85
	Key clearance, μm	-100	-100	-100	150	150	150	150	150	150
	Collaring force, MN	34	34	34	20	16	20	20	10	10
	Collar nose stress at max. collaring force ^a , MPa	—	-227	-195	-264	-217	-195	-169	-137	-151
	Collar nose stress after keys insertion ^a , MPa	—	-186	-134	-195	-160	-97	-105	-86	-80
De-collaring	Stopper height, including shims, mm	70.1	69.85	69.85	69.85	69.85	69.85	69.85	69.85	69.85
	De-collaring force, MN	34	16	16	20	16	8	9	—	—

^a Average over the four strain gauges located in the center of the magnet.

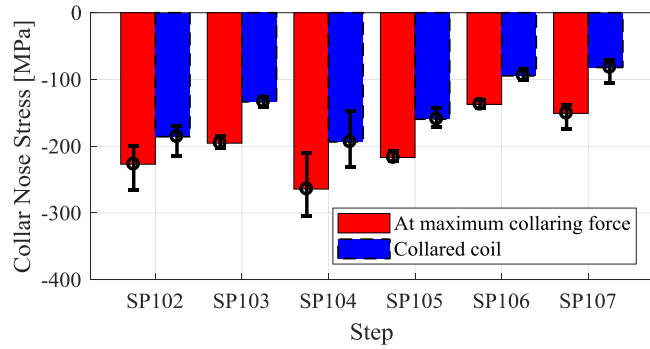


Figure 11. Stress measured on the collar nose averaged over the four strain gauges in central part of the magnets. Error bars show the maximum and minimum measured stress.

The updated collaring procedure consists of placing a shim of 1 mm between the stoppers, press until contact is reached over the full length and the cavity is 70.7 mm. Then the pressure is removed, the thickness of the shim is reduced and the procedure is repeated. The keys are inserted at a collaring cavity of 69.85 mm, using a collar tool shim of 0.15 mm. By reducing the tool shim gradually, the pressure transferred to the collar-coil assembly is increased gradually, and the coil assembly is gently massaged. Most importantly, by controlling the displacement of the collars we ensure that no excessive forces are applied.

7.2. Collaring spring back

While the collars are under the collaring press, the collar arms are almost stress free. After key insertion, when the collaring press is released, the collars spring back from zero into tension. Figure 12 shows the correlation plot between the collar nose stress at the maximum collaring force and after releasing the collaring press. Measurements from all instrumented collars are included in the plot. In average, the measured spring back in the collar nose is 60 MPa, which corresponds to an average coil stress of about 30 MPa. This is partially due to the clearance needed for keys insertion and partially due to the deformation of the collars [11]. A way to quantify the deformation of the collars is to measure the dimension of the collared coils along the pole axis and mid-plane axis. Measurements of the collared coil diameter performed in several short model magnets reveal a deviation from the nominal values in the axis of the poles, but close to nominal dimension along the mid-plane axis: the collared coil assembly is elliptically deformed. The vertical deflection of the collared coil is proportional to the coil pack azimuthal excess. Figure 13 shows the measured collared coil deflection measured in different longitudinal positions of the magnet axis as a function of the coil pack excess. Measurements are compared to the computed vertical deflection, assuming at Young’s modulus of the coil blocks is 20/40 GPa, respectively at loading and unloading. According to the FE model, yoking and cool down has a negligible impact on the collared coil elliptical deformation.

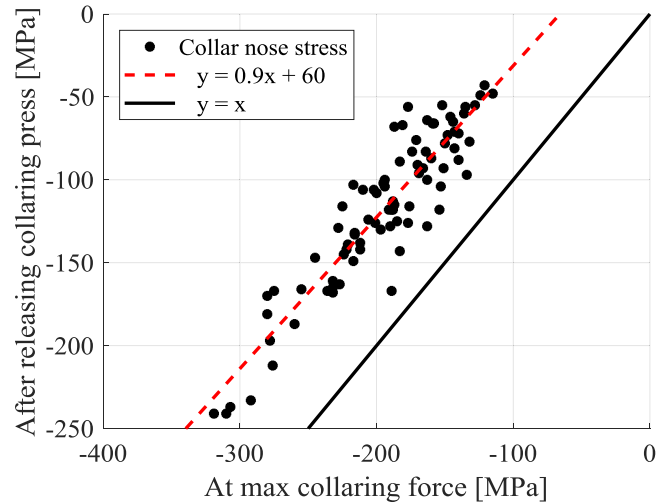


Figure 12. Correlation plot between the collar nose stress at the maximum collaring force and after releasing the collaring press for all 11 T collared coil assemblies.

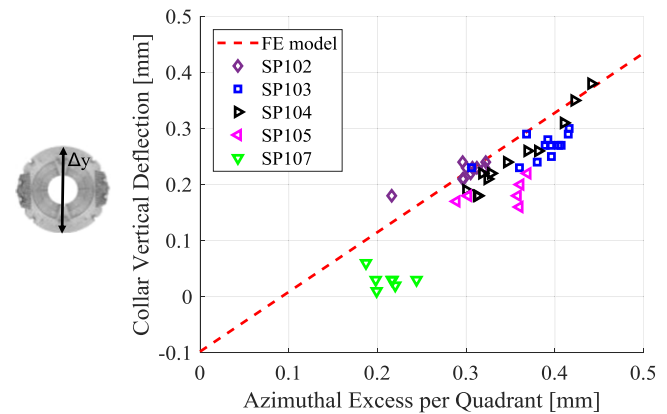


Figure 13. Measurement of collared coil deviation from nominal as a function of the azimuthal coil package excess per quadrant. The dashed line shows the expected FE predictions.

7.3. Impact of azimuthal variation on the coil size along the magnet longitudinal axis

The coils produced in the 11 T program have a significant variation of their azimuthal size along the coil length; therefore, it is crucial to study its effect on the pre-stress in the various assembly steps. As SP105 is the assembly with most varying coil package azimuthal size, it is used as a study case for the consequences of its size variation by analysis of mechanical and magnetic data. The coil package of SP105 have a local azimuthal excess of 0.450 mm per quadrant in the center of the magnet (at $z = 650$ mm, where z is the position in the straight section relative to the pole key). The size decreases significantly towards the ends by over 150 μ m. At $z = 50$ mm, the coil package size per quadrant is 0.300 mm.

The longitudinal variation of pre-stress is captured by the strain gauge measurements on the collar nose placed in three longitudinal locations (see figure 14). At max collaring force,

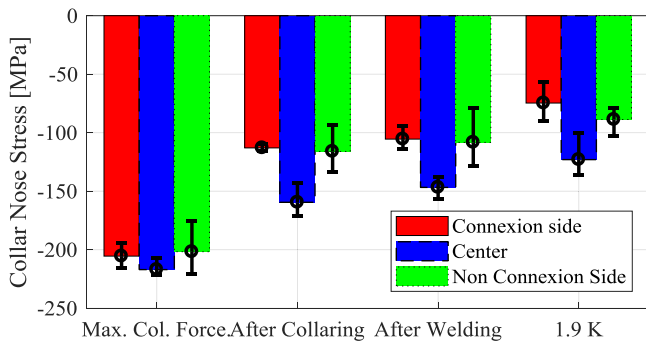


Figure 14. Stresses measured in the collar nose strain gauges in three segments of the straight section of SP105. Error bars show the maximum and minimum stress measured in the four-instrumented collars for each magnet longitudinal position.

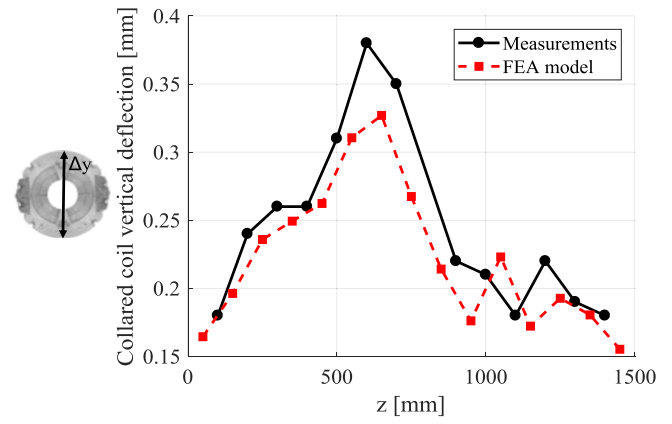


Figure 16. Measurement of collared coil deviation from nominal along the pole axis along the length of the straight section (z) of SP105. The deviation is well captured by FE modelling (dashed line).

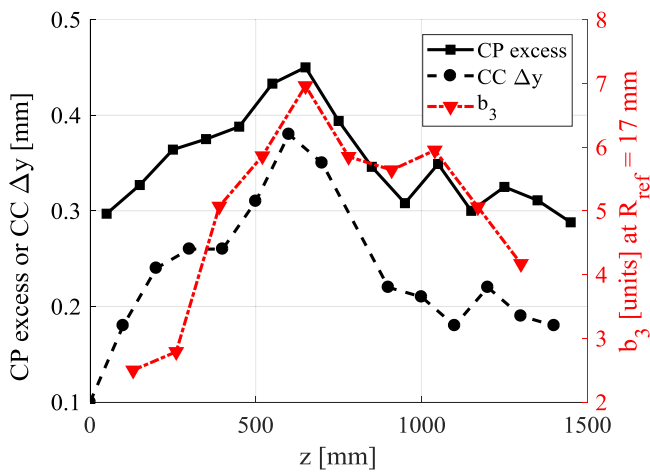


Figure 15. Measured coil package (CP) excess per quadrant, collared coil vertical deflection (CC Δy) and the sextupole component (b_3) of the field harmonics in SP105 along the magnet axis.

the stresses are 13 MPa higher in the center as compared to the extremities. Once collared, the stresses are 45 MPa higher in the center gauges. In the following cold mass assembly and cool down, the difference is 40 MPa between center and the magnet ends.

The variation of coil azimuthal size along the magnet axis is also visible in the collared coil geometric and magnetic measurements. The vertical deflection of the collared coil is expected to be larger in the regions with larger coil pack excess. Figure 15 compares the measured coil package excess per quadrant with the measured vertical deflection of the collared coil and the measured sextupole component (b_3) of the field. In figure 16, the measured collared coil vertical deflection is compared to the expected deformation from the FE model. The actual coil size and shimming layout is modelled. The predicted difference in collared coil size between the lowest excess region ($z = 50$ mm) and the highest excess region ($z = 650$ mm) is 0.16 mm, in good agreement with the measurements. The azimuthal stresses in the coil are enhanced in the more oversized region. This effect is not visible in SSC dipoles [11] due to the lower rigidity of

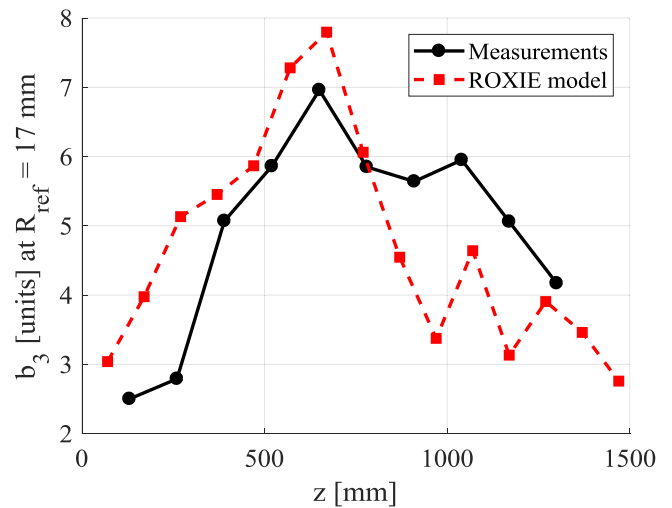


Figure 17. Comparison of the sextupole component of the field harmonics in SP105, measured at room temperature, at a reference radius of 17 mm. The measurements are compared to calculations in ROXIE including the vertical deflection of the collared coil along the magnet length.

the coils and the use of tapered keys. Magnetic measurements performed on the cold mass assembly at room temperature confirmed the collared coil deformation along the magnet axis, with a variation of the sextupole component of 4.5 units. Figure 17 compares the measured and expected sextupole due to the elliptic deformation of the collared coil given by the local coil package azimuthal excess. The field harmonics are modelled in ROXIE by introducing the vertical deflection in the collared coil as an elliptical deformation of the winding mandrel. Field measurements were performed on the cold mass assembly meaning that even in the surrounding structure (yoke and shell), the shape of the collared coil remains. Therefore, the cold mass assembly has a negligible effect on the relative pre-stress along the magnet axis. Without this feature in the cold mass assembly, stresses would be more elevated in the high azimuthal excess regions.



Figure 18. Collared coil enclosed in the laminated yoke before shell welding.

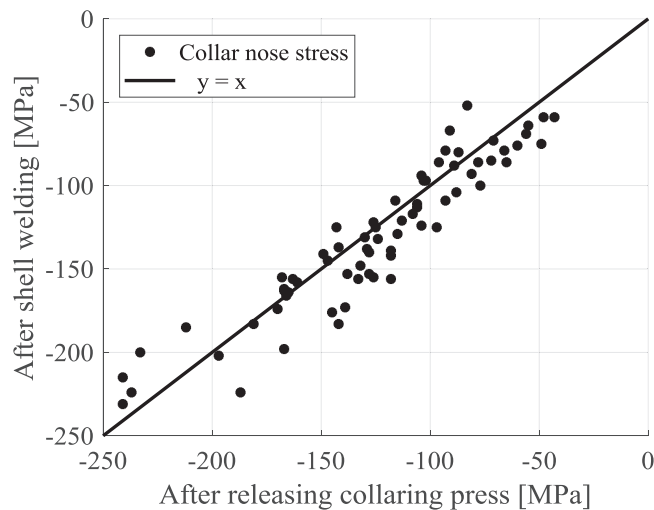


Figure 19. Correlation plot between the collar nose stress after collaring and after shell welding for all 11 T single aperture cold mass assemblies.

8. Cold mass assembly

Yoke laminations are placed around the collared coils, and the assembly is enclosed in stainless steel shells of 10 mm for single aperture and 15 mm for the double aperture magnets (see figure 18). Figure 19 shows the measured collar nose stresses for the structure after shell welding compared to the stresses after collaring. The shell welding modifies the collar nose stress on average by ± 10 MPa with respect to the stresses of the collared coil. According to the FE model, cold mass assembly has a marginal effect on the stresses measured by the collar nose strain gauges.

The final step in the magnet assembly is the welding of the end plates followed by longitudinal loading. Longitudinal forces are monitored using four bullet gauges per aperture.

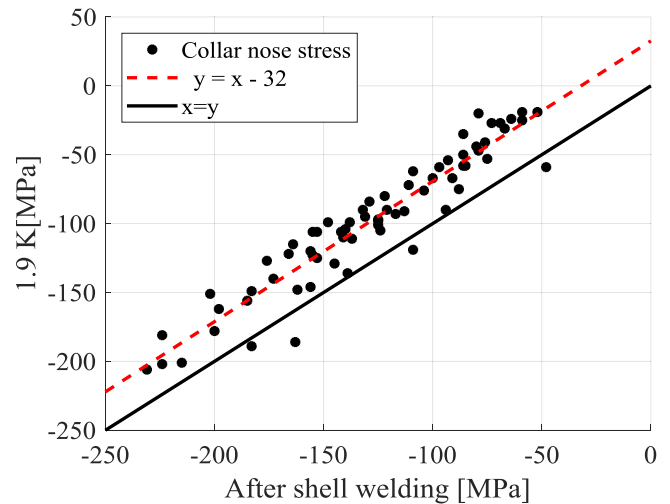


Figure 20. Correlation plot between the collar nose stress after shell welding and after cool down for all 11 T cold mass assemblies.

These are special screws machined to accommodate a cylindrical piece, called bullet, on which strain gauges are mounted to measure the force exerted by the coil against the end plate. The coils are loaded longitudinally by 30–60 kN per aperture (7%–14% of the longitudinal electromagnetic force at nominal current) with the purpose of maintaining a contact between the coil and the end plate after cool down, providing a rigid longitudinal support to the coil (that will tend to expand due to the axial component of the Lorentz force).

9. Cool down and powering

As the magnets are cooled down from ambient temperature to 1.9 K, the stress measured by the strain gauges is reduced due to thermal shrinkage differentials between the various cold mass components. On average, the collar nose stress released is 30 MPa. Figure 20 shows the correlation plot from all the strain gauges in the magnets, comparing the state after shell welding to the state at 1.9 K. The dashed line represents the best fit of the measured data fixing the slope to 1. In order to match the average measured change of stress during cool down, the integrated coil contraction in the FE model had to be increased from 3.6 mm m^{-1} [19] to 4.2 mm m^{-1} . The value is close to the 3.9 mm m^{-1} coil thermal contraction derived for MQXF [33]. The coil elastic modulus is assumed to be the same at 1.9 K and room temperature.

When the magnets are powered, the Lorentz forces in the coils are directed towards the mid-plane. The stresses in the collar nose reduces linearly with the square of the current, i.e. the applied forces. For the magnets in the earlier stage of the short model program (SP102–SP105) the strain gauge data during powering is in general noisy. For the test of DP102 an effort was made to update the data acquisition system to get a clean signal. Therefore, there is only reliable data for DP102, SP106 and SP107. Figures 21–22 show the stress evolution in

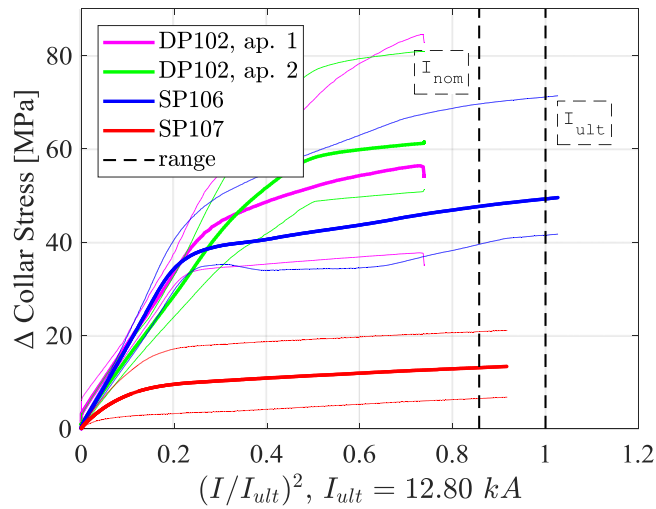


Figure 21. Collar nose stresses in SP106, SP107 and the two apertures of DP102 during powering in the straight section of the magnet. The dashed line marks the nominal (11.85 kA) and ultimate (12.85 kA) current.

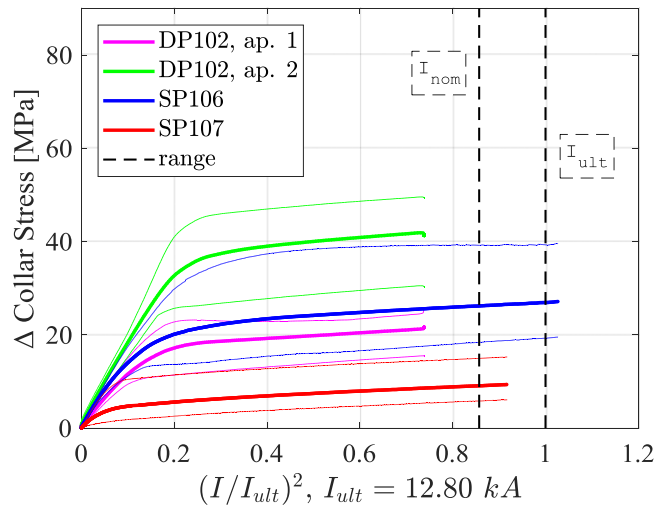


Figure 22. Collar nose stresses in SP106, SP107 and the two apertures of DP102 during powering in the connection side of the magnet. The dashed line marks the nominal (11.85 kA) and ultimate (12.85 kA) current.

the collar nose with the square of the current for the two apertures of DP102, SP106 and SP107, averaged over the four-instrumented collars per location. The plots show the connection side and the central gauge read out separately. The curves are shifted to zero stress at 0 kA. Initially the stresses decrease linearly with the applied forces. At a certain current level, the rate with which the stresses release slows down significantly, and a flattening of the curves occur. The behavior is reproduced quench after quench. The gradual reduction of stress between the pole and the coil is typical for cosine-theta magnets, where the electromagnetic forces act towards the mid-plane, opposite to the forces given by the pre-load as has been observed in SSC and LHC model magnets and prototypes. The flattening of the curves indicates

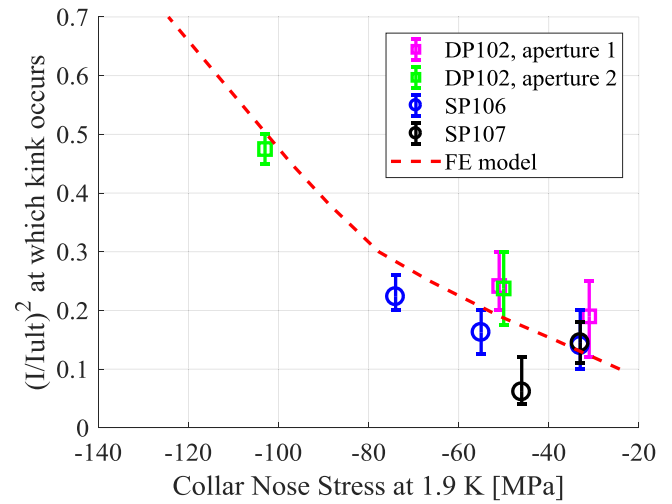


Figure 23. The result of the strain gauge measurements during powering are summarized for magnets SP106, SP107 and the two apertures of DP102. The level of current squared reached before the slope change occurs in the strain gauge curves is plotted against the stresses at 1.9 K, and compared to the finite element prediction. The error bar represents the spread of the slope change of the four strain gauges at each location.

an unloading of the collar nose where the strain gauges are located. In the absence of direct measurements, this cannot be confirmed. The change of the slope does not appear to limit the performance of the magnets, as it occurs at much lower current than the maximum current. For example, in SP106 it occurs at $0.2(I/I_{ult})^2$, which is round 6 kA, i.e. less than half of the max current reached. This does not prevent the magnet from reaching the ultimate current. From the short model program, the mid-plane limitation has proven to be a hard limit. The loss of collar nose pre-compression, however, does not appear to limit the performance at ultimate current. The flattening of the strain gauge curve for SP107 occurs at even lower current. SP107 had the fastest training to ultimate current, at which stable operation has been demonstrated. The level of azimuthal pre-stress in this magnet seems to be sufficient to ensure performances up to ultimate current and can be used as a reference for the 11 T program. However, the long term behavior of the magnet still needs to be confirmed through endurance tests (this will be done on SP109).

The current square at which the slope change occurs is different from magnet to magnet. Compiling the current square at which the slope change occurs for magnets DP102, SP106 and SP107 seems to exhibit a correlation with the measured stresses in the collar nose after cool down and zero current (see figure 23). Higher stresses at cold indicate that the slope change in the strain gauge curves at powering will occur at higher applied forces. The dashed line corresponds to the current level at which the slope of the collar nose stress changes for a given collar nose stress after cool down according to the FE model, which corresponds to a loose of pre-compression between pole and coil. More data points in the future will hopefully help clarify the trend. As mentioned, the strain gauge data in the magnets SP102-SP105 are noisy. It is worth mentioning though, that in some ramps, there are

Table 8. Shell traction stress after welding and cool down for the short model magnets with instrumented shells.

Magnet	After welding [MPa]	After cool down [MPa]	Δ [MPa]
SP101	400	520	120
SP103	305	525	220
SP107	260	470	210
DP101	225	350	125
DP102	250	390	140

certain strain gauges signals clean enough for a slope change to be visible. In the strain gauge data of SP104, the magnet with the highest pre-load, these slope remains linear with respect to the current squared, during its entire current ramp.

Five of the magnets (SP101, SP103, SP107, DP101 and DP102) have strain gauges on the inner and outer radius of the shell. Table 8 summarizes the measured shell traction stress after welding and after cool down and figure 24 shows the stress evolution on the shell as a function of the square of the currents. The very modest change of stress on the shell compared to the average is a confirmation that the electromagnetic forces are well contained by the yoke providing a very rigid support to the collared coil assembly.

The measured longitudinal force by the bullet gauges, per aperture, is presented in figure 25. The magnet is loaded longitudinally by 30–60 kN per aperture at room temperature. During cool down, 50% of the pre-load is lost. During powering, around 35% of the electromagnetic forces is transferred to the bullet gauges. The remaining part is held by the coil and the frictional contacts in the system.

10. Discussion

The collar nose strain gauge data in all assembly steps and cool down for all single aperture magnets are summarized in figure 26. The error bars correspond to the standard deviation of the 12 strain gauges in each magnet. The overall behavior of each magnet during the various assembly steps is rather reproducible, except for the inconsistent procedure of the collaring, which was detailed in section 7. Unusually high delta stress from the assembly at max collaring force to the collared coil, so-called relaxation, of 75 MPa on average is observed for SP104 and SP105. This can be explained by the excessive force that was introduced in the system at the max collaring force in these two magnets (see table 7).

The effect of cool down is rather predictable across the magnets, with the exception of SP102, where a higher stress loss was observed. The general behavior of SP102 is the most deviating magnet. For a magnet with low targeted pre-stress (see table 4), the measured stresses are rather high through the entire assembly process. The residual stress at 1.9 K are expected to be proportional to the azimuthal excess of the coil package of the magnets. In some occasions, a discrepancy between the targeted and effective pre-stress is observed. SP106 and SP107 are the magnets with the lowest stresses in

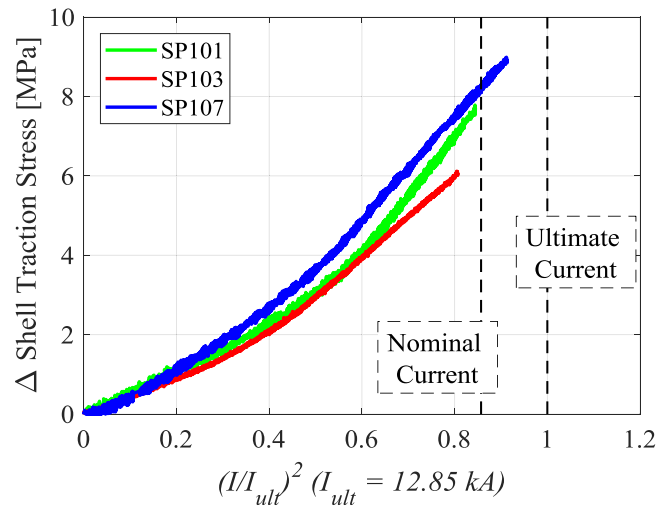


Figure 24. Shell traction stress in the single aperture magnets as a function of the square of the current.

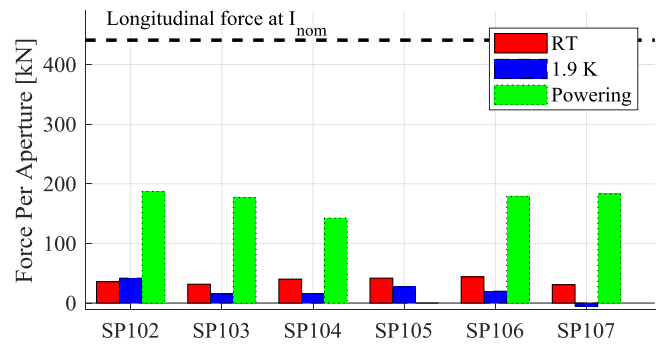


Figure 25. Measured forces over the four bullet gauges per aperture at room temperature, 1.9 K and at powering. The horizontal lines mark the total electromagnetic forces at the nominal current.

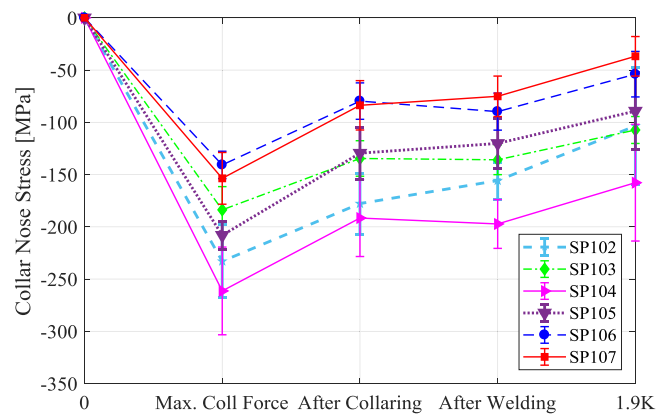


Figure 26. Summary of collar nose strain gauge measurements at the assembly steps for all single aperture models. The error bars correspond to the standard deviation of the 12 strain gauges in each magnet.

the collar nose at 1.9 K. The stresses at 1.9 K of SP106 are on a similar level as SP107 even if the azimuthal excess is 0.1 mm lower. A possible explanation is that the collars in SP106 were reused from the disassembled SP105. Measurements on these collars after the test in SP105 show that the inner diameter of these collars were increased compared to the

nominal values by up to 60 μm . The magnet with the largest azimuthal coil package excess, SP104, is indeed the magnet with the highest stresses at cold. On the other hand, SP102, SP103 and SP105 had similar collar nose stresses at 1.9 K, even though the coil package size in SP102 is significantly smaller, both on average and in its local maximum.

11. Conclusions

For the 11 T, as in all Nb_3Sn magnets, it has become clear that it is critical to control the size of the coils and limit the maximum stress in the mid-plane. Cable insulation was re-optimized, decreasing the thickness to limit coil over-compression and enlarging the mica coverage to reduce the stress concentration at the cable edges. A review of the collaring procedure of the 11 T magnet was launched with the goal of reducing the risk of conductor degradation due to stress observed in three short model magnet. In the new collaring procedure, the collaring tool shim is gradually reduced based on measured displacements, minimizing the force required to insert the keys. In order to limit the peak stress during collaring to 150 MPa, the maximum excess per quadrant is 0.3 mm. All the new features were implemented in the short model magnet SP107, which reached ultimate current after five training quenches.

Variations of coil size leads to varying stresses in the conductor, as well as variation in the dimensions of the collared coil. In particular, an elliptical deformation is observed in the collared coils, which scales with the local size of the coil package. This observation of the collared coil is validated by finite element modelling, which in addition suggests that the enhanced ellipticity in the region of more oversized coil package remains in all the following assembly steps and cool down. Mechanical measurements show that the relative stress variation along the magnet length remain through all assembly steps and cool down. It is therefore clear that varying coil sizes have consequences for the mechanical state of the magnet during assembly, cool down and powering.

Mechanical data from six single aperture magnets (MBHSP102–MBHSP107) and two double aperture magnets (MBHDP101 and MBHDP102) is compiled and analysed. Clean and reliable strain gauge data at powering gives an insight in the mechanical state of the coils during magnet excitation. The initial stress at 0 kA decreases linearly with the applied forces during powering. At a certain current level the loss rate of stress decreases significantly. This is interpreted as a signature of loss of compression on the collar nose which does not appear to limit the performance at ultimate current. The current square at which the slope change occurs

is different from magnet to magnet. For the least preloaded magnet, SP107, the flattening of the curve occurs almost from start, at about 10% of the ultimate current squared, this does not prevent SP107 to have the fastest training out of all short models and to achieve ultimate current. Endurance of the 11 T magnets under such condition still has to be assessed. SP107 is also the first model assembled with coils using the final conductor and insulation layout with larger mica coverage to reduce the stress concentration at the cable edges. The less compacted cavity during reaction and impregnation minimizes the risk of damaging the coil during fabrication. Last but not least, collaring was performed in a controlled manner with a maximum excess per quadrant of 0.250 mm, assuring the peak stress during collaring is below 150 MPa. On the other hand, there are strong indications that excessive mid-plane stresses may limit the operation of the 11 T dipoles. SP104, SP105 and DP102 were all limited at operation below ultimate current. For DP102, the coils were likely permanently damaged at room temperature during collaring, as reducing the pre-stress as compared to SP104 and SP105 (from which the coils were reused) did not improve the magnet performance.

The marginal increase of the shell stress during powering demonstrates that the electromagnetic forces are well contained by the yoke, providing a very rigid support to the collared coil structure. A small longitudinal load is applied on the magnet during room temperature assembly in order to guarantee that the coil is in contact with the end plates after cool down, providing a rigid support structure for the longitudinal magnetic forces. Around 35% of the electromagnetic force is transferred to the bullet gages. The rest is held by the coil and the friction among components.

Acknowledgments

The authors would like to thank CERN technical staff for contributions to magnet design, construction and test. They are also grateful to Mikko Karppinen, Bernhard Auchmann, David Smekens and Alexander Zlobin for their work in the design and construction of the 11 T magnet and the useful discussions.

Appendix

The quench curves of all single aperture and double aperture models are shown in figures A1–A9.

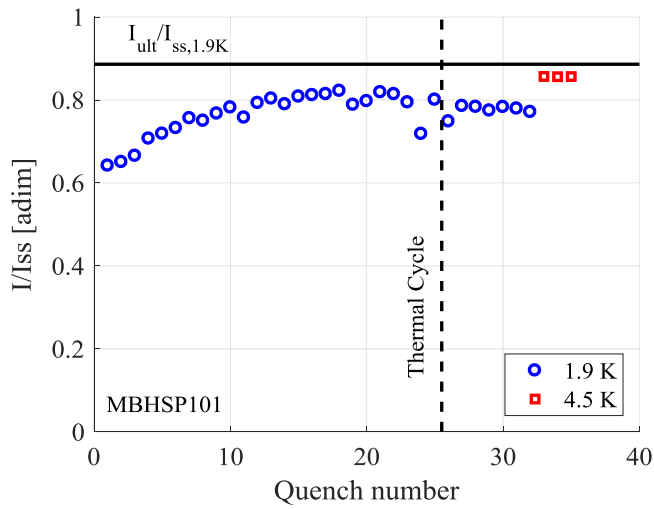


Figure A1. Training plot of 11 T MBHSP101 single aperture short model with nominal ramp rate (10 A s^{-1}).

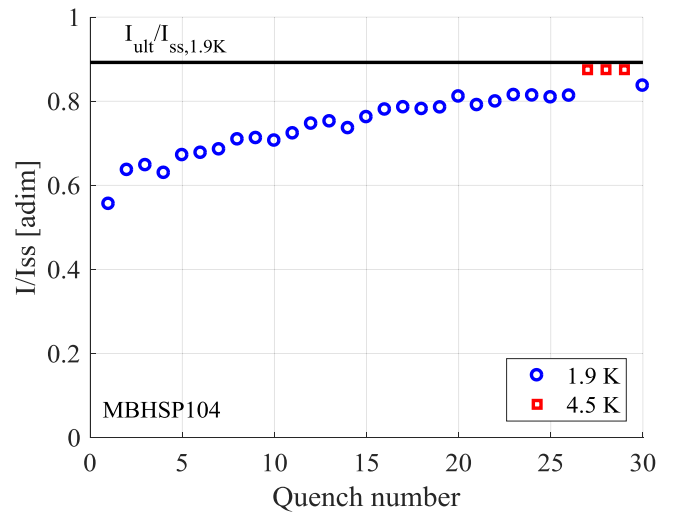


Figure A4. Training plot of 11 T MBHSP104 single aperture short model with nominal ramp rate (10 A s^{-1}).

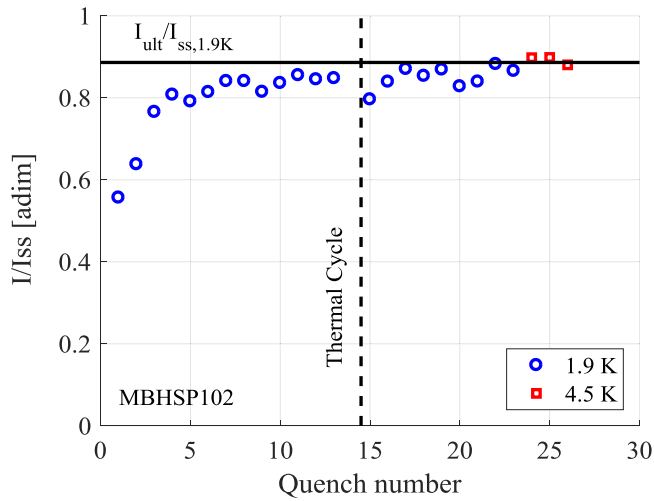


Figure A2. Training plot of 11 T MBHSP102 single aperture short model with nominal ramp rate (10 A s^{-1}). The magnet was not ramped above ultimate current.

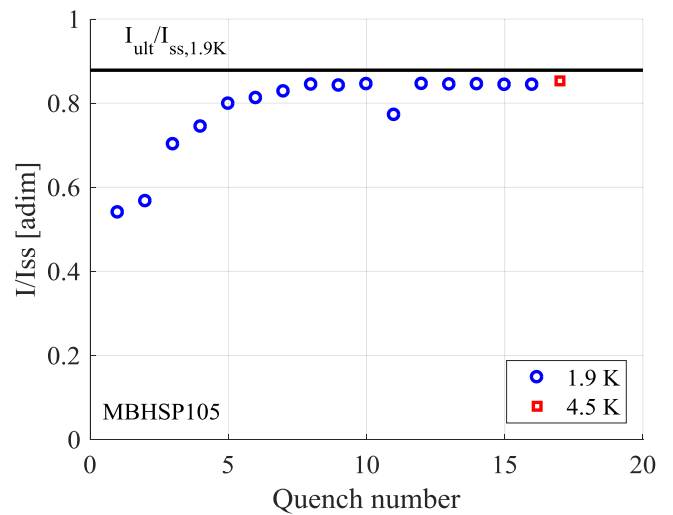


Figure A5. Training plot of 11 T MBHSP105 single aperture short model with nominal ramp rate (10 A s^{-1}).

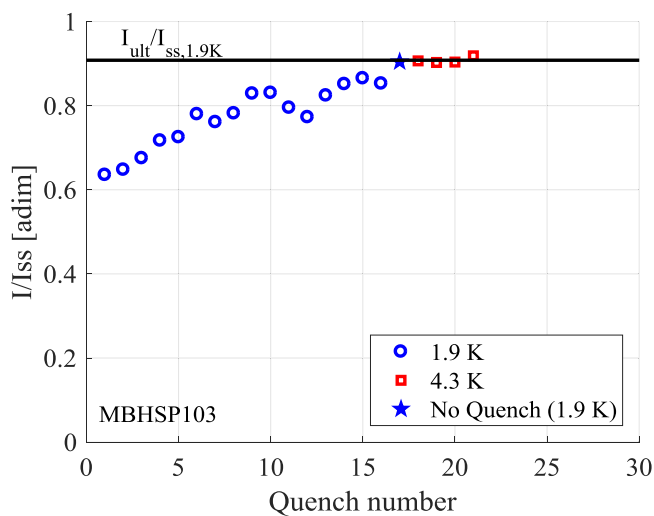


Figure A3. Training plot of 11 T MBHSP103 single aperture short model with nominal ramp rate (10 A s^{-1}). The magnet was not ramped above ultimate current.

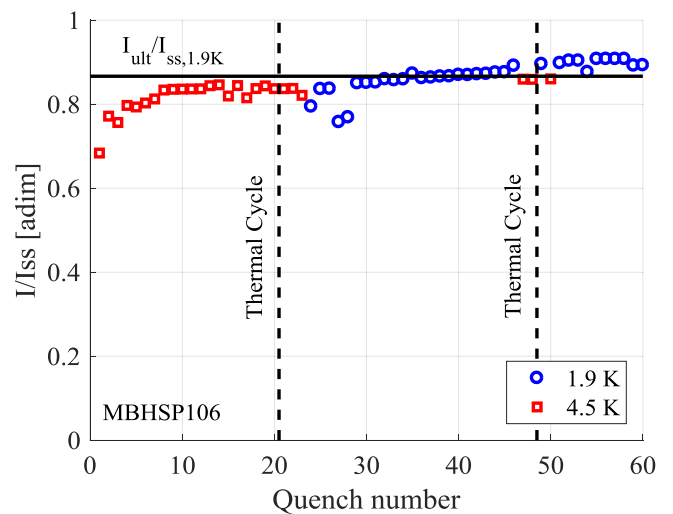


Figure A6. Training plot of 11 T MBHSP106 single aperture short model with nominal ramp rate (10 A s^{-1}).

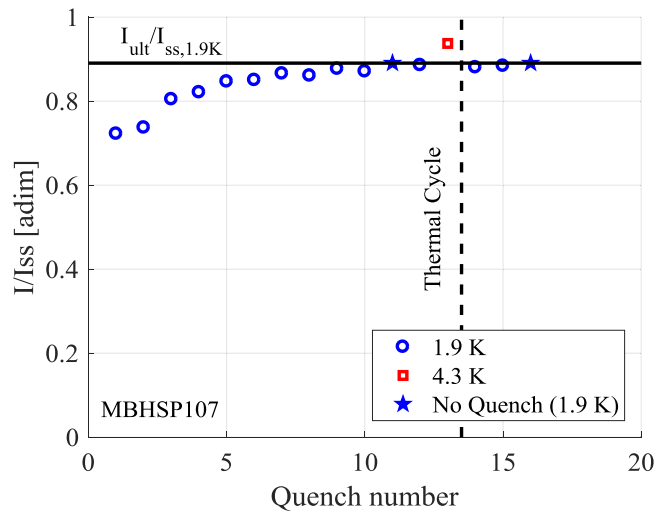


Figure A7. Training plot of 11 T MBHSP107 single aperture short model with nominal ramp rate (10 A s^{-1}). The magnet was not ramped above ultimate current.

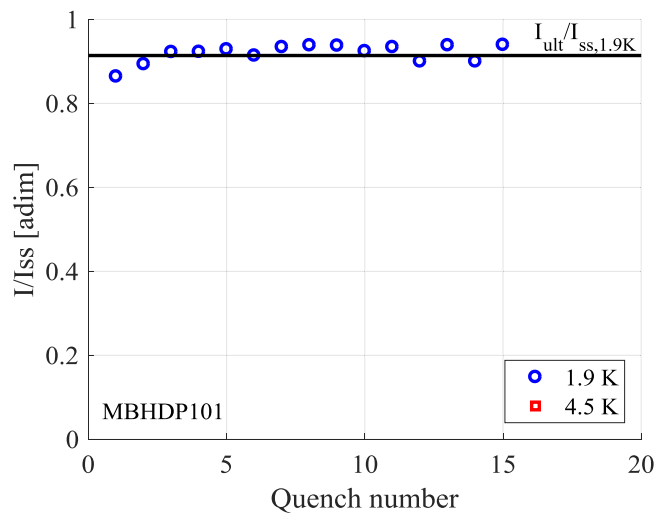


Figure A8. Training plot of 11 T MBHDP101 double aperture short model with nominal ramp rate (10 A s^{-1}).

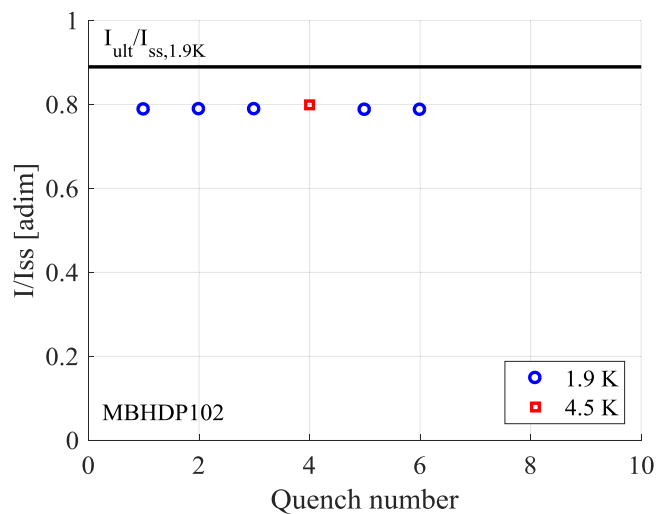


Figure A9. Training plot of 11 T MBHDP102 double aperture short model with nominal ramp rate (10 A s^{-1}).

ORCID iDs

S Izquierdo Bermudez <https://orcid.org/0000-0003-2157-4751>

C Löffler <https://orcid.org/0000-0003-0033-7052>

References

- [1] Apollinari G, Bejar Alonso I, Brüning O, Lamont M and Rossi L 2015 High-Luminosity Large Hadron Collider (HL-LHC): preliminary design report *CERN Yellow Reports Monographs* (Geneva: CERN)
- [2] Bottura L *et al* 2012 Advanced accelerator magnets for upgrading the LHC *IEEE Trans. Appl. Supercond.* **22** 4002008
- [3] Karppinen M *et al* 2012 Design of 11 T twin-aperture dipole demonstrator magnet for LHC upgrades *IEEE Trans. Appl. Supercond.* **22** 4901504
- [4] Zlobin A V *et al* 2012 Design and fabrication of a single-aperture 11 T Nb₃Sn dipole model for LHC upgrades *IEEE Trans. Appl. Supercond.* **22** 4001705
- [5] Ekin J W 1980 Strain scaling law for flux pinning in practical superconductors: I. Basic relationship and application to Nb₃Sn conductors *Cryogenics* **20** 611–24
- [6] Ekin J W 1987 Effect of transverse compressive stress on the critical current and upper critical field of Nb₃Sn *J. Appl. Phys.* **62** 4829–34
- [7] Bordini B, Alknes P, Ballarino A, Bottura L and Oberli L 2014 Critical current measurements of high-Jc Nb₃Sn Rutherford cables under transverse compression *IEEE Trans. Appl. Supercond.* **24** 9501005
- [8] Koepke K *et al* 1979 Fermilab doubler magnet design and fabrication techniques *IEEE Trans. Magn.* **MAG-15** 658–61
- [9] Wolff S 1992 Superconducting magnet design *AIP Conf. Proc.* **249** 1160–97
- [10] Anerella M *et al* 2003 The RHIC magnet system *Nucl. Instrum. Methods* **A499** 280–315
- [11] Devred A 1992 About the mechanics of SSC dipole magnet prototypes *AIP Conf. Proc.* **249** 1309
- [12] Ogitsu T *et al* 1993 Mechanical performance of 5 cm aperture, 15 m long SSC dipole magnet prototypes *IEEE Trans. Appl. Supercond.* **3** 686–91
- [13] Brüning O *et al* 2004 *LHC Design Report* (Geneva: CERN) p 548
- [14] Ferracin P *et al* 2014 Magnet design of the 150 mm aperture low- β quadrupoles for the high luminosity LHC *IEEE Trans. Appl. Supercond.* **24** 4002306
- [15] Tommasini D *et al* 2018 Status of the 16T dipole development program for a future hadron collider *IEEE Trans. Appl. Supercond.* **28** 4001305
- [16] Tollestrup A V 1984 Superconducting magnet technology for accelerators *Annu. Rev. Nucl. Part. Sci.* **34** 247–84
- [17] Asner A *et al* 1989 First, 1m long superconducting dipole model magnets for LHC break the 10 tesla field threshold *Proc. MT-11 (Tsukuba, Japan)*
- [18] den Ouden A *et al* 1994 An experimental 11.5 T LHC type dipole magnet *IEEE Trans. Magn.* **30** 2320
- [19] Löffler C, Daly M, Savary F and Nilsson E 2018 Finite element analysis of the mechanical conditions of the Nb₃Sn cable of the 11T dipole magnet during operation *IEEE Trans. Appl. Supercond.* **28** 4008105
- [20] Willering G *et al* 2018 Comparison of cold powering performance of 2 m long Nb₃Sn 11 T model magnets *IEEE Trans. Appl. Supercond.* **28** 4007205
- [21] Fleiter J and Lackner F 2018 private communication

- [22] Troitino J F *et al* 2018 Applied metrology in the production of superconducting model magnets for particle accelerators *IEEE Trans. Appl. Supercond.* **28** 4002106
- [23] Ferracin P *et al* 2019 Mechanical analysis of the collaring process of the 11T dipole magnet *IEEE Trans. Appl. Supercond.* **29** 4002705
- [24] Willering G 2016 Cold powering tests of 11-T Nb₃Sn dipole models for LHC upgrades at CERN *IEEE Trans. Appl. Supercond.* **26** 4005604
- [25] Willering G *et al* 2017 Cold powering performance of the first 2 m Nb₃Sn DS11T twin-aperture model magnet at CERN *IEEE Trans. Appl. Supercond.* **27** 4002505
- [26] Bermudez S I *et al* 2019 Quench protection study of a 11T Nb₃Sn model dipole for the high luminosity LHC *IEEE Trans. Appl. Supercond.* **29** 4701005
- [27] Bajas H *et al* 2018 Advanced Nb₃Sn conductors tested in racetrack coil configuration for the 11T dipole project *IEEE Trans. Appl. Supercond.* **28** 4008605
- [28] Fernández J L R *et al* 2019 Characterization of the mechanical properties of Nb₃Sn coils *IEEE Trans. Appl. Supercond.* **29** 8401205
- [29] Jimenez N and Sgobba S Characterization of discup C3/30 ODS copper alloy for 11T DS dipole from f Luvata OY/ECKA granules *CERN EDMS Report* 1216580 (CERN)
- [30] Bordini B *et al* 2012 Impact of the residual resistivity ratio on the stability of Nb₃Sn magnets *IEEE Trans. Appl. Supercond.* **22** 4705804
- [31] Ferracin P *et al* 2019 The HL-LHC low- β quadrupole magnet MQXF: from short models to long prototypes *IEEE Trans. Appl. Supercond.* **29** 4001309
- [32] Borgnolutti F *et al* 2009 Reproducibility of the coil positioning in Nb₃Sn magnet models through magnetic measurements *IEEE Trans. Appl. Supercond.* **19** 1100–5
- [33] Vallone G *et al* 2017 Mechanical performance of short models for MQXF, the Nb₃Sn low- β quadrupole for the Hi-Lumi LHC *IEEE Trans. Appl. Supercond.* **27** 4002906